Dust and pollution aerosols over the Negev desert, Israel: Properties, transport, and radiative effect

Yevgeny Derimian,[1] Arnon Karnieli,[1] Yoram J. Kaufman,[2] Meinrat O. Andreae,[3]
Tracey W. Andreae,[3] Oleg Dubovik,[2] Willy Maenhaut,[4] Ilan Koren,[5] and Brent N. Holben[2]

[1] The complex spatial, temporal, and optical characteristics of atmospheric aerosols cause large uncertainties in the estimation of aerosol effects on climate. Analysis of long-term measurements from key regions can provide a better understanding of the role of atmospheric aerosols in the climate system. In the current study, observations of aerosol optical properties and mass concentrations were carried out during 1995–2003 in the Israeli Negev desert. The measurement site is relatively remote from local pollution sources; however, it lies at the crossroad between dust from the Sahara and the Arabian peninsula and pollution from Europe. The instruments employed were a Sun/sky photometer, a stacked filter unit sampler, and an integrating nephelometer. We analyzed the data for seasonal variability, general vertical aerosol structure, and radiative climate effect by dust and anthropogenic aerosol. The intra-annual variability of aerosol optical properties was found to be closely related to seasonally varying synoptic conditions. Two seasonal peaks of aerosol optical thickness were noted: The first maximum related to dust particle activity and the second to anthropogenic aerosol. Similar maximums were noted in aerosol light scattering at the surface; however, their relative importance is reversed and is related to differences in the vertical distribution of dust and anthropogenic aerosols. The calculated aerosol radiative effect shows cooling both at the top of the atmosphere and at the surface during the whole year. The radiative effect of the airborne dust is the dominating forcing component during most of the time in the study area.

1. Introduction

[2] Aerosol particles affect the climate system directly by scattering and absorbing solar radiation and indirectly by changing cloud properties. The amount of reflected and absorbed radiation influences the energy balance of the surface-atmosphere system, thereby modulating evaporation rate and cloud formation [*Charlson et al.*, 1992; *Hansen et al.*, 1997; *Kaufman et al.*, 2002]. Aerosols also enhance the concentration of cloud condensation nuclei, leading to an increase in cloud albedo, and can either suppress or in some cases increase precipitation [*Kaufman and Fraser*, 1997; *Levin et al.*, 1996; *Menon et al.*, 2002; *Rosenfeld et al.*, 2001]. In addition, desert dust, biomass smoke, and anthropogenic air pollutants affect visibility and air quality, as well as human health [*Chu et al.*, 2003; *Lelieveld et al.*, 2002; *Wang and Christopher*, 2003].

[3] It has been noted in numerous recent papers that the eastern Mediterranean basin is characterized by relatively high levels of tropospheric aerosol due to the influence of anthropogenic aerosols, originating mainly from Europe, and mineral dust from the North African, Sinai, and Saudi Arabian deserts [*Andreae et al.*, 2002; *Formenti et al.*, 2001a; *Gerasopoulos et al.*, 2003; *Ichoku et al.*, 1999; *Israelevich et al.*, 2003; *Kubilay et al.*, 2003]. *Andreae et al.* [2002] attribute most of the pollution aerosol observed in the southeast Mediterranean to long-range transport from Central and Eastern Europe, as well as from Southern Russia. *Ganor* [1994] provides dust episode statistics on the basis of records of horizontal visibility, concentration of suspended dust, and the amount of dust settling conducted over a period of 33 years (1958/1959 to 1990/1991) in Tel Aviv. For this period he reports 621 dust episodes and shows that the probability for a dust episode to occur increases from fall to winter, rises to a peak in April, and decreases sharply toward summer. *Ganor and Foner* [2001] carried out individual particle

[1]Remote Sensing Laboratory, Jacob Blaustein Institute for Desert Research, Ben-Gurion University of the Negev, Sede Boker Campus, Israel.
[2]NASA Goddard Space Flight Center, Greenbelt, Maryland, USA.
[3]Biogeochemistry Department, Max Planck Institute for Chemistry, Mainz, Germany.
[4]Department of Analytical Chemistry, Institute for Nuclear Sciences, Ghent University, Ghent, Belgium.
[5]Department of Environmental Sciences, Weizmann Institute, Rehovot, Israel.

analysis of aerosol collected in Tel Aviv and Jerusalem, Israel.

[4] Two intensive field campaigns focusing on the physical, chemical, and light-scattering characteristics of aerosols were conducted at Sede Boker (in some sources mentioned as Sde Boker) in the Negev desert of Israel. The first took place during the summer (20 June to 10 July 1996) [*Formenti et al.*, 2001b], and the second in the winter (18 February to 15 March 1997) [*Ichoku et al.*, 1999]. Both experiments were carried out under the "Aerosol Radiation and Chemistry Experiment" (ARACHNE) program. Individual particles and their sources were also characterized in the framework of this program [*Sobanska et al.*, 2003].

[5] Continuous measurements of total column atmospheric optical properties (by means of a Sun/sky photometer), monitoring of surface scattering coefficients (by means of an integrating nephelometer), and collection of airborne particles (by means of an aerosol sampler) have been conducted at the Sede Boker site sporadically since 1990 [*Kaufman et al.*, 1994] and continuously since 1995 [*Andreae et al.*, 2002; *Maenhaut et al.*, 1997; *Maenhaut et al.*, 1996b]. These long-term observations have enabled researchers to compile representative statistics in order to evaluate aerosol optical properties and radiative effect.

[6] The current study, on the basis of observations of the above mentioned three instruments, is aimed at analyzing the optical and physical properties of the aerosols in the Negev desert and their temporal dynamics over a period of about seven years. Further, the research provides an assessment of the vertical structure of aerosol transport along with calculations of the dust and anthropogenic pollution radiative effects.

2. Site Description

[7] All measurements were conducted at the Sede Boker Campus of Ben-Gurion University of the Negev (30°51′N, 34°47′E, 470 m above mean sea level (msl)), Israel. Sede Boker is located in the northern part of the Negev desert, relatively far from highly populated and industrial areas. The northern Negev is characterized by a dry climate, with mean annual precipitation of 100–200 mm and 20–40 rainy days throughout the year. The annual average temperature is 17–19°C, ranging from 32°C in August to 6°C in January. The average relative humidity at 14:00 local time for July is 30–35% and for January, 40–50% [*Stern et al.*, 1986].

[8] From a synoptic point of view, a typical year in the Negev desert can be subdivided into four seasons. Winter (mid-November to the end of March) is the rainy season, characterized by the activity of migrating cyclones and anticyclones. Spring (April and May) is essentially a transition period into the summer (June–September), which is characterized by a semipermanent low-pressure trough extending from the Persian Gulf to the Negev region. During spring, hot low-pressure troughs that have developed along the North African coast can move rapidly into Israel through Egypt. Hot and clear days with minimal day-to-day variations prevail in summer; wind from the north-west is dominant and usually increases in the daytime because of a sea breeze. Fall (October to mid-November) is a short transition period between the monotonous summer and the winter [*Stern et al.*, 1986].

[9] The atmospheric boundary layer (ABL) has been characterized by studies conducted in Israel by *Dayan and Rodnizki* [1999] on the basis of three years (1987–1989) of soundings conducted by the Israeli Meteorological Service. At nighttime, a radiative inversion leads to the development of a stable boundary layer, which reaches its maximum depth of about 425 m (based on 05:00 and 23:00 UT soundings) during the spring and the beginning of the summer. The thickness of the nocturnal stable layer drops sharply to about 300 m in August and remains at this value for the rest of the year. The frequency of occurrence of a stable layer drops from April to August. This stable boundary layer mainly causes an increase in pollution concentration during the night and early morning.

[10] The mixed layer represents the largest part of the convective boundary layer. This layer lies above the free convective layer (which reaches 60–150 m above the surface), and is capped by the entrainment layer (thickness about 100 m), which separates the mixed layer from the stable free atmosphere aloft. The mixed layer generally contains vertically well-mixed pollutant concentrations. During the summer in the study region, this layer is governed by large-scale synoptic conditions known as the "Persian trough", when diurnal variations are driven only by surface heat fluxes and the daily sea breeze cycle. The reported monthly mean depth of the mixed layer, for all diurnal soundings, shows a distinctive minimum of ∼700–900 m during May–August, then an increase from ∼1,000 to ∼1,600 m from September to October. During winter, it remains in the range between ∼1,600 to 1,900 m until about the middle of March, and then gradually drops during April. Information on the vertical dynamics of the mixed layer gives us an estimation of a possible pollution vertical profile.

3. Instrumentation and Data Sets

[11] The data sets were obtained from (1) a CIMEL Sun/sky photometer, part of the global Aerosol Robotic Network (AERONET); (2) a single-wavelength integrating nephelometer; and (3) a "Gent" PM10 stacked filter unit (SFU) sampler.

3.1. AERONET

[12] The AERONET program is an automatic robotic Sun and sky scanning measurement initiative [*Holben et al.*, 1998]. The CIMEL spectral radiometer performs direct Sun measurements every 15 min, with a 1.2° field of view at 340, 380, 440, 500, 675, 870, 940, and 1020 nm nominal wavelengths. The spectral aerosol optical thickness (τ_{ext}) was retrieved at seven of these wavelengths from direct to Sun measurements; the 940 nm channel was used to retrieve water vapor content. The angular distribution of sky radiance was also measured at 440, 670, 870 and 1020 nm. The measured spectral Sun and sky radiances were used to retrieve aerosol optical parameters at four wavelengths by the AERONET inversion code [*Dubovik and King*, 2000], which uses models of homogeneous spheres and randomly oriented spheroids. For fine mode aerosol (Ångström parameter > 0.6) we used a spherical model by setting 5% sky radiance fitting error criteria, and for coarse mode aerosol (Ångström parameter ≤ 0.6) we used a spheroids model

with a fitting error of 10% or better. According to recommendations of the AERONET group for reliability of the inversion product, the following restrictions were also applied: (1) the number of the symmetrical scattering angles in inverted almucantar should be equal to or higher than 21; (2) the minimal solar zenith angle should range between 25 and 77°; and (3) additional criteria applied to retrieved data of single-scattering albedo, which require minimal solar zenith angle of 45° and minimal τ_{ext} at 440 nm of 0.4. More details on the retrieval algorithm and accuracy assessments can be found in work by *Dubovik and King* [2000], *Dubovik et al.* [2000, 2002a, 2002b], and *Smirnov et al.* [2000].

3.2. Nephelometer

[13] The Integrating Nephelometer (M903, Radiance Research, Seattle, WA, USA) measures the light scattering extinction coefficient (σ_{scat}) with a 2 min resolution at a wavelength of 545 nm, with a scattering angular range of $7°-170°$. The instrument is operated indoors and air is supplied through plastic tubing of up to 3 m length and of 2.2 cm internal diameter. The inlet of the tubing is located outdoors at about 10 m above ground level and faces downward. Pressure, temperature, and relative humidity (RH) in the scattering volume of the instrument are also monitored and recorded. In order to eliminate a nonlinear increase in σ_{scat} due to high humidity, the data with RH > 80% were removed [*Andreae et al.*, 2002].

[14] Two similar nephelometers were operated successively at the site during the study period, using the same wavelength. Both instruments were calibrated after set up in the field, and then a series of calibration procedures with particle-free air and CO_2 as a span gas were periodically conducted during the measurement period. The first instrument was set up in October 1997 and operated until August 1999. According to *Formenti et al.* [2001a], for this period 3 calibrations were performed and calibration coefficients were stable within 3%. The second instrument was set up in November 1999 and operated until November 2003, during which time 7 calibration procedures were conducted in which the calibration coefficients were stable within 6%.

[15] An additional source of uncertainty is the truncation of near-forward and backward scattered light, which causes underestimation of the total scattering coefficient. This truncation uncertainty is also particle size–dependent. In order to correct for the truncation error, information on particle size is needed. The truncation error for a three-wavelength Nephelometer TSI 3563 was found to be <10% for fine mode particles and to increase up to $20-50\%$ for the coarse mode [*Anderson et al.*, 1996]. *Anderson and Ogren* [1998] suggest a correction equation based on the observed Ångström parameter, but since we used the Integrating Nephelometer M903 with a single wavelength, such a correction is not applicable. However, on the basis of data published by *Andreae et al.* [2002], which was obtained from a three-wavelength Nephelometer TSI 3563 with the same scattering angular range of $7°-170°$, that operated at Sede Boker from December 1995 until October 1997, it can be seen that the truncation correction of the mean scattering coefficient is about 15% at 550 nm. It should be noted that this correction was obtained for a relatively dusty year (1996).

3.3. "Gent" PM10 Stacked Filter Unit Sampler

[16] The "Gent" PM10 stacked filter unit (SFU) sampler collects particles in a coarse ($2-10$ μm aerodynamic diameter (AD)) and fine (<2 μm AD) size fractions. The SFU sampler is operated continuously on a two-two-three-day scheme. The instrument was located at about 8 m above the ground and operated at an air flow rate of $\sim12-16$ L/min. To avoid the problem of nonrepresentative measurements in the two-two-three-day scheme, the sampling was always conducted with a timer set at 50% for the two-day sample and at 33% for the three-day sample, thus the SFU effectively sampled only 50 or 33% of the time evenly distributed over two or three days, respectively. This should yield generally little clogging or effects from a decrease in flow rate during the sampling, except for maybe episodes of extremely high aerosol concentrations. The SFU samples were analyzed for particulate mass (PM), black carbon, and over 40 elements. In this study, only the PM concentration in the coarse and fine size fractions was used; it was measured using gravimetry and is given in μg/m^3 at standard temperature and pressure. The uncertainty associated with the weighing is usually less than 3% for the coarse PM and less than 5% for the fine PM. The volume of the sampled air is obtained from a volume meter, which is accurate within 5% and does not depend on the concentration of the aerosol in the air. Thus the total uncertainty of the measured PM concentration is expected to be about 6% for coarse and 7% for fine PM. More details about the SFU samples and the chemical elements analysis, including studies conducted at the Sede Boker site have been discussed by *Maenhaut et al.* [1996a, 1996b, 1997] and *Andreae et al.* [2002].

3.4. Back Trajectories

[17] Five-day air mass backward trajectory analysis was obtained from the 3-D HYSPLIT (HYbrid Single-Particle Lagrangian Integrated Trajectory) model made available by the U. S. National Oceanic and Atmospheric Administration (NOAA) [*Draxler and Hess*, 1998]. Calculations were performed at 500, 2500 and 5000 meters above ground level using the global reanalysis meteorological data set. The lowest level of 500 m was chosen to be indicative of surface air mass origin, and the upper level of 5000 m to represent high-altitude long-range aerosol transport.

3.5. Study Duration

[18] The AERONET observations analyzed covered the period from January 1996 to November 1996 and from February 1998 to April 2002. For a specific analysis, the data set from July 2002 to November 2003 was added; these data were automatically cloud screened, but were not subjected to final calibration, and therefore are not yet quality assured. The nephelometer measurements analyzed here were carried out from January 1998 to December 2003. The "Gent" PM10 SFU sampler data set included a period of observations from January 1995 to July 2001.

4. Results, Analysis, and Discussion

4.1. Climatology of Aerosol Optical Properties

4.1.1. Seasonal Characteristics

[19] A summary of the aerosol observations at Sede Boker is presented in Table 1. Figure 1 illustrates the mean

Table 1. Summary of Aerosol Observations at the Sede Boker Site[a]

	Jan	Feb	March	April	May	June	July	Aug	Sept	Oct	Nov	Dec	Overall
$\tau_{ext}(500)$	0.18 ± 0.12	0.15 ± 0.10	0.19 ± 0.11	0.25 ± 0.15	0.22 ± 0.11	0.16 ± 0.06	0.24 ± 0.11	0.24 ± 0.09	0.21 ± 0.08	0.22 ± 0.09	0.18 ± 0.09	0.11 ± 0.06	0.20 ± 0.11
$\mathring{a}(870/440)_{weighted}$	1.01 ± 0.66	0.99 ± 0.64	0.79 ± 0.51	0.59 ± 0.44	0.57 ± 0.33	0.94 ± 0.44	0.92 ± 0.33	1.18 ± 0.48	0.93 ± 0.44	1.03 ± 0.52	0.95 ± 0.52	1.06 ± 0.56	0.91 ± 0.51
WV, g/cm²	1.07 ± 0.38	0.94 ± 0.29	1.12 ± 0.27	1.17 ± 0.32	1.46 ± 0.39	1.50 ± 0.37	1.87 ± 0.44	2.10 ± 0.49	2.07 ± 0.42	2.04 ± 0.42	1.42 ± 0.40	1.15 ± 0.36	1.55 ± 0.58
Observations/months	942/6	1742/7	2681/7	1699/7	2180/5	3188/6	3058/7	3998/7	3642/7	1921/6	1154/6	1129/5	27334/76
C_{vf} μm³/μm²	0.019 ± 0.015	0.018 ± 0.015	0.024 ± 0.018	0.031 ± 0.025	0.028 ± 0.019	0.025 ± 0.017	0.029 ± 0.026	0.033 ± 0.024	0.024 ± 0.017	0.026 ± 0.020	0.027 ± 0.019	0.017 ± 0.013	0.027 ± 0.021
C_{vc} μm³/μm²	0.046 ± 0.051	0.061 ± 0.062	0.074 ± 0.058	0.131 ± 0.087	0.135 ± 0.098	0.066 ± 0.044	0.094 ± 0.076	0.074 ± 0.07085	0.090 ± 0.068	0.111 ± 0.093	0.107 ± 0.118	0.042 ± 0.032	0.097 ± 0.075
Observations/months	47/3	55/3	128/6	104/5	150/5	136/5	168/6	193/6	246/6	121/4	10/2	33/3	1016/45
$\sigma_{scat0}(545)$, Mm⁻¹	52 ± 42	57 ± 58	63 ± 71	63 ± 81	57 ± 66	66 ± 55	69 ± 47	78 ± 53	55 ± 41	59 ± 44	61 ± 52	51 ± 45	60 ± 56
Observations/months	1.3 × 10⁵/6	1.1 × 10⁵/6	1.2 × 10⁵/6	1.0 × 10⁵/6	1.0 × 10⁵/5	1.2 × 10⁵/6	1.3 × 10⁵/6	1.1 × 10⁵/6	1.1 × 10⁵/5	1.1 × 10⁵/5	1.2 × 10⁵/6	1.3 × 10⁵/6	13.9 × 10⁵/69
FPM, μg/m³	15 ± 6	14 ± 5	15 ± 5	15 ± 6	16 ± 4	16 ± 3	17 ± 4	18 ± 5	14 ± 4	13 ± 3	15 ± 5	15 ± 6	15 ± 5
CPM, μg/m³	39 ± 51	47 ± 93	57 ± 105	58 ± 78	48 ± 51	35 ± 15	34 ± 16	30 ± 10	38 ± 27	35 ± 28	46 ± 35	48 ± 45	43 ± 57
Samples/months	79/7	91/7	100/7	88/7	91/7	94/7	86/7	80/6	70/6	81/6	76/6	80/6	1016/79

[a]Mean values are accompanied by associated standard deviation.

monthly variability of the Aerosol Optical Thickness (AOT or τ_{ext}), at 500 nm, the Ångström parameter (å), and water vapor content (WV) during the study period. The Ångström parameter represents the wavelength dependence of scattering on particle size and is calculated by

$$\mathring{a} = -\frac{\ln \frac{\tau_{ext}^{870}}{\tau_{ext}^{440}}}{\ln \frac{\lambda^{870}}{\lambda^{440}}}, \qquad (1)$$

where λ is the wavelength and the superscript numbers indicate the respective spectral bands in nm. In this study, the average value of å was calculated by weighting it by τ_{ext}^{500}.

[20] Figure 1 reveals two periods with relatively high values of τ_{ext}, the first during April–May and the second during July–October. The first period fits the spring synoptic definition. The weighted monthly mean values of å for April and May are the lowest at 0.59 ± 0.44 and 0.57 ± 0.33, respectively, and indicate a significant presence of large particles, corresponding to high dust storm activity.

[21] The second period matches the summer season and the beginning of fall according to the synoptic definition. This is the dry season, characterized by high water vapor (WV) due to a higher temperature regime and the air masses arriving mainly from the Mediterranean Sea. The AERONET measurement analysis shows that the peak of the mean WV values reaches 2.1 ± 0.5 g/cm² in August, while in April and May it is 1.17 ± 0.3 and 1.46 ± 0.4 g/cm², respectively. The northwest wind during the summer penetrates the Negev, bringing humidity and air masses from the densely populated industrial coast of central Israel as well as from Europe. In this season, å increases and reaches a monthly mean maximum of 1.18 ± 0.5 in August. These high values occur along with an increase in τ_{ext}, and correspond to dominant fine particle loading with anthropogenic origin. The winter months (mid-November to
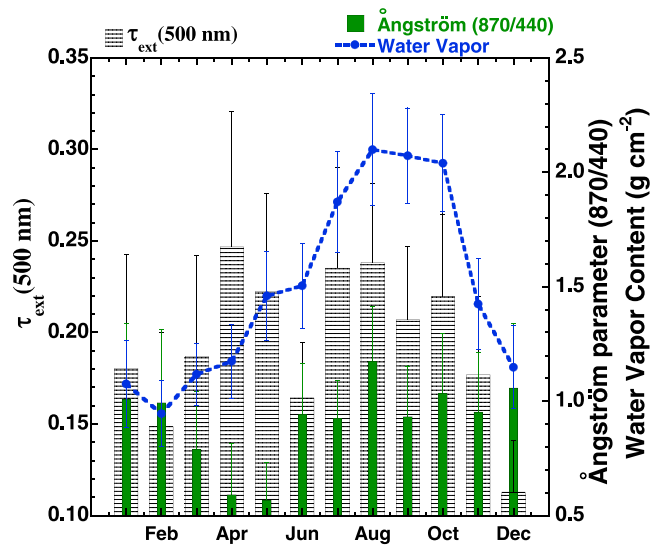

Figure 1. Monthly mean values of τ_{ext} at 500 nm, water vapor content, and Ångström parameter. Vertical bars indicate standard deviation.
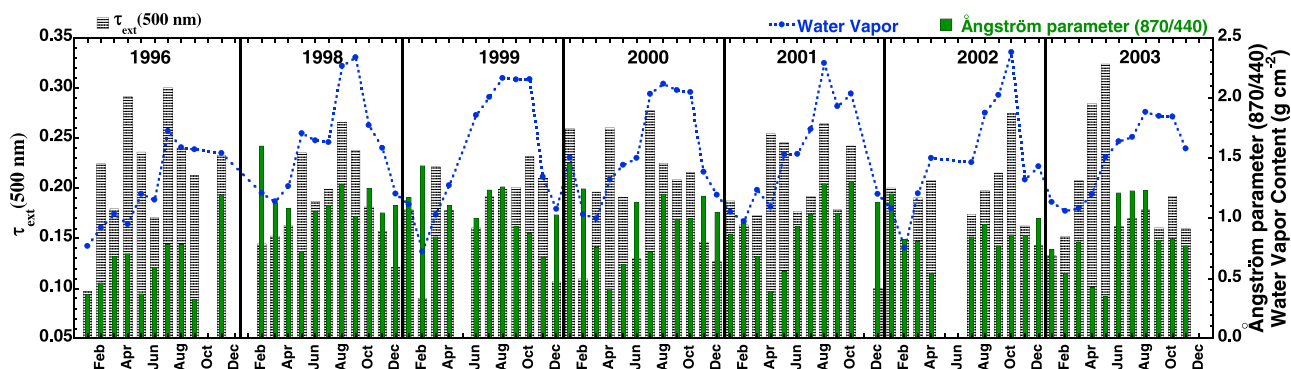
Figure 2. Year-to-year variability of monthly mean τ_{ext} at 500 nm, water vapor content, and Ångström parameter.

March), which are the rainy season, are characterized by clean atmospheric conditions with a lower monthly mean of τ_{ext}.

4.1.1.1. Interannual Variability

[22] The temporal variability throughout the entire study period is shown in Figure 2, where the general year-to-year behavior of the aerosol optical parameters is similar to the monthly mean-averaged data shown in Figure 1, that is, increased τ_{ext}, accompanied by low Ångström parameter values in the spring and higher values in the summer during 1996, 1998, 2000, and 2001. The water vapor content had a periodic pattern throughout the entire period, with an increase during the summer months. 1996 was relatively dry (lowest water vapor content) and dusty (lowest Ångström parameter values). No long-term trend is evident during the period of observations.

4.1.1.2. Histogram Analysis

[23] Figure 3 shows the frequency of occurrence histogram analysis of τ_{ext} for different ranges of å. The histogram analysis is based on daily means of τ_{ext} and å for the entire study period. We classified events with å < 0.5 as dust, events with a range of 0.5 < å < 1.0 as mixed aerosols, and those with å > 1.0 as anthropogenic pollution. The τ_{ext} histograms show a peak around 0.15 to 0.2. As the å values decrease, the histograms decline slowly, which shows dominant dust contribution to the high τ_{ext}. Also, τ_{ext} was slightly more affected by mixed aerosols than by pure pollution. Events for which 1.5 < å < 2 virtually did not contribute to high τ_{ext}.

4.1.1.3. Single-Scattering Albedo

[24] The single-scattering albedo (ω_0), which reflects the absorption characteristics of the aerosol, is defined as

$$\omega_0 = \frac{\sigma_{scat}}{\sigma_{scat} + \sigma_{abs}}, \qquad (2)$$

where σ_{scat} and σ_{abs} are scattering and absorption coefficients, respectively. The average optical properties of tropospheric aerosol types, retrieved from AERONET measurements at various locations [Dubovik et al., 2002a] show patterns for spectral ω_0. Urban, industrial, and biomass-burning aerosols absorb more radiation at longer wavelengths, while desert aerosols absorb stronger in the blue spectral range. Both patterns of spectral ω_0 have been observed at Sede Boker, in spite of its desert location.

[25] The analysis of ω_0 is limited to observations that fulfill the criteria of a minimum solar zenith angle of 45° and a minimum τ_{ext} at 440 nm of 0.4, which are required to provide accurate (±0.03) values of ω_0 according to Dubovik et al. [2002a]. This restriction reduces the data series and prevents us from obtaining a complete data set for monthly mean analysis. However, some reliable data for several months can serve as representative samples and hint at the seasonal pattern of the spectral ω_0 (Figure 4a). Spectral ω_0 indicates an anthropogenic pollution pattern for August and dust dominance for all other represented months. Generally, it is worth noting that the observed aerosols are low absorbing. The decreasing level of the spectral ω_0 from March to May is accompanied by an increase of the related mean values of τ_{ext}(440 nm) and a decrease of the related mean values of Ångström parameter. Such a trend can be due to increasing intensity of dust storms. Considering the average values and the standard errors of the measured spectral ω_0, two general spectral absorption characteristics can take place, namely, dust or anthropogenic pollution dominated. Further, these general spectral absorption char-
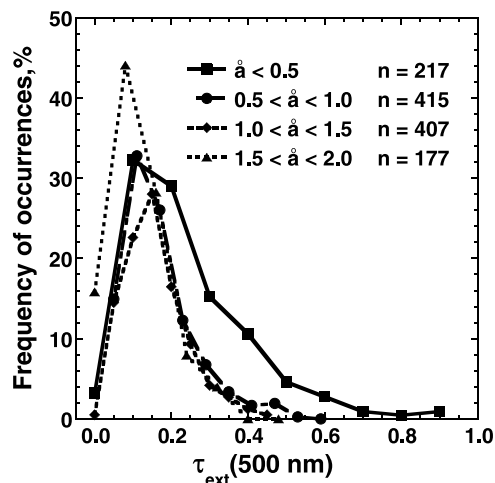

Figure 3. Frequency of occurrence histograms of τ_{ext} at 500 nm for different ranges of the Ångström parameter (870/440), å. The histograms are based on the daily mean data; n is the number of analyzed days.
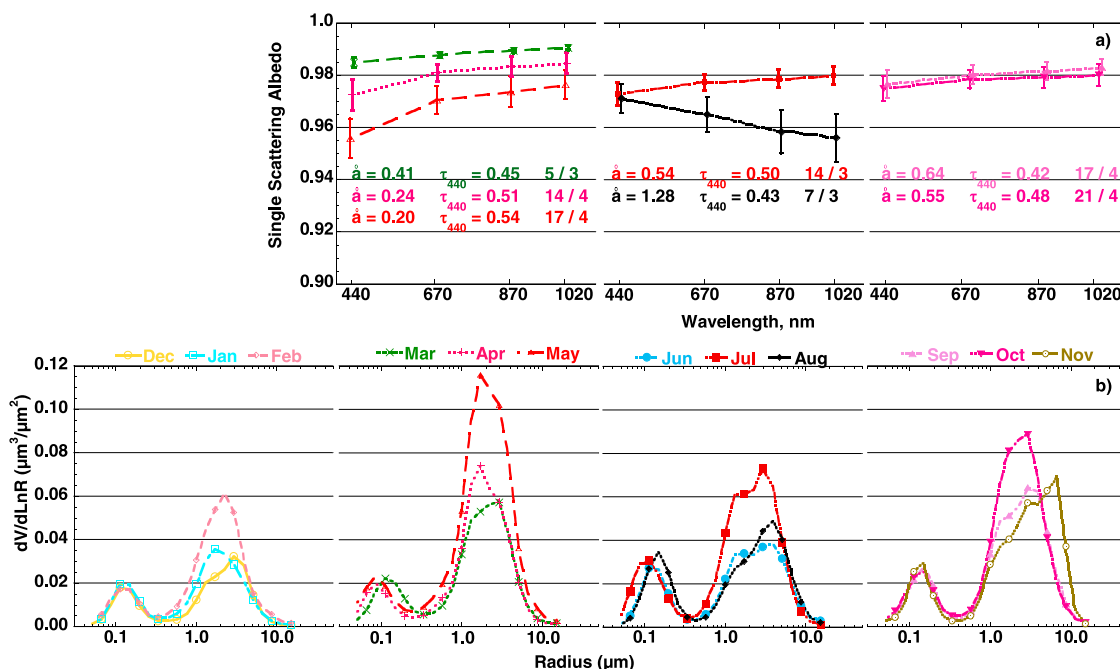
Figure 4. (a) Representative monthly values of spectral ω_0 measurements. Note that these values should be considered as representative values rather than monthly means because of a relatively small number of observations. The data are accompanied by related mean values of Ångström parameter, å; aerosol optical thickness at 440 nm, τ_{440}; and number of days/number of years analyzed. Vertical bars indicate standard error. (b) Monthly mean aerosol volume size distribution. The mean values were calculated by weighting them by aerosol optical thickness.

acteristics of dust and pollution can be used for calculating the aerosol radiative effect.

4.1.1.4. Volume Size Distribution

[26] The averaged aerosol volume size distribution, $dV(r)/d\ln r$, and the associated particle volume concentration (C_v), as a numerical characteristic, are presented in Figure 4b and in Table 1, respectively. C_v is calculated as

$$C_v = \int_{r_{\min}}^{r_{\max}} \frac{dV(r)}{d\ln r} d\ln r. \qquad (3)$$

[27] Figure 4b reveals that despite the month to month variability, the coarse fraction ($0.6 < r_c < 15\ \mu m$) dominates throughout the entire year. Note that the increase of the coarse fraction from March to May follows a decrease in the level of the spectral ω_0, as mentioned above. The fine fraction ($0.05 < r_f < 0.6\ \mu m$) remains almost constant from December to May suggesting a background level; however, it increased noticeably during the summer. A relative increase in the fine fraction during August is accompanied by a simultaneous decrease in the coarse fraction pointing out a dominating role of the fine aerosols in that month. Some of the increase in the coarse fraction during the winter was due to irregular individual dust storm events. The monthly mean aerosol volume size distribution in Figure 4b was calculated by weighting it by aerosol optical thickness. A comparison of the volume size distribution, retrieved by the AERONET inversion, with other measurements techniques can be found, for example, in work by *Reid et al.* [2003].

4.1.1.5. Surface Level Observations

[28] The obtained total column aerosol properties can be compared to the surface level aerosol as obtained by the filter sampling and the ground base integrated nephelometer measurements.

[29] The analysis of the filters provides monthly mean coarse particulate mass (CPM; 2–10 μm aerodynamic diameter, AD) and fine particulate mass (FPM; AD < 2 μm) concentrations (Table 1 and Figure 5). During the dust-dominated spring season the CPM relative contribution to the surface aerosol increases. The CPM decreases in the summer with a minimum in August. The FPM relative contribution to the surface aerosol showed the inverse behavior, with a maximum in August.

[30] The monthly mean total scattering coefficient at the surface (σ_{scat0}), measured by the integrating nephelometer, also shows substantial seasonal variability (Figure 6). During the summer, the monthly mean σ_{scat0} reaches a maximum of $78 \pm 53\ Mm^{-1}$ in August, while in April there is a secondary maximum of $63 \pm 81\ Mm^{-1}$. The minimum values of the monthly mean σ_{scat0} are $51 \pm 45\ Mm^{-1}$ and $52 \pm 42\ Mm^{-1}$ during December and January, respectively.

[31] Next we compared the aerosol optical characteristics at the surface and the total integrated atmospheric column. While the seasonal maxima in aerosol light scattering at the surface (σ_{scat0}) and column-integrated extinction τ_{ext} coincide, their relative importance is reversed, with σ_{scat0} showing the highest values in summer and τ_{ext} peaking in spring. These differences in the seasonal features of surface and column-integrated data are related to differences in the aerosol vertical distribution. Dust is dominating at higher
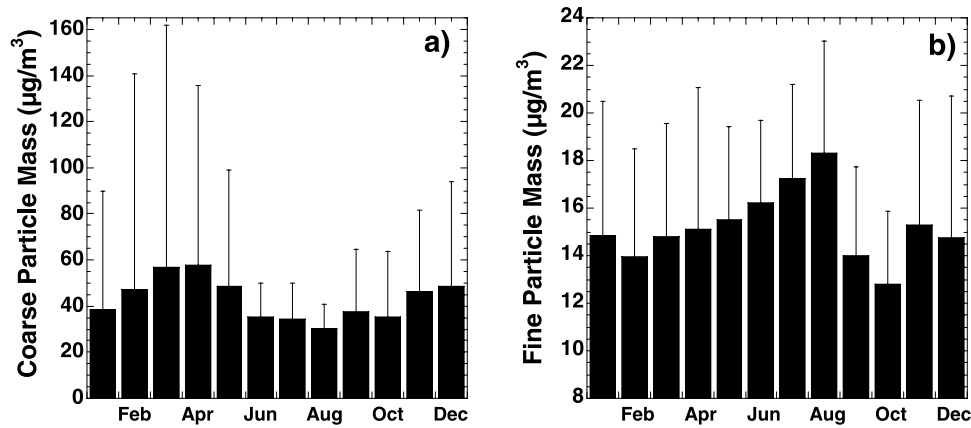
Figure 5. (a) Coarse (aerodynamic diameter of $2-10\ \mu\text{m}$) and (b) fine (aerodynamic diameter of $<2\ \mu\text{m}$) particulate mass concentration obtained by in situ particle sampling at the surface ("Gent" SFU). Vertical bars indicate standard deviation.

altitudes and anthropogenic aerosol is more abundant at low altitudes. An additional discussion on this issue is presented in the next section.

4.1.2. Estimation of Aerosol Vertical Profile Features

[32] Information about aerosol vertical profiles (variation of aerosol loading with altitude) is rare for the eastern Mediterranean region. The sporadic observations point out a wide range of altitudes where mineral dust is present, from 1.5 to 5 km or even up to 7 and 8 km [*Alpert et al.*, 2004; *di Sarra et al.*, 2001; *Hamonou et al.*, 1999; *Tsidulko et al.*, 2002]. Pollution concentrations at altitudes between 1 and 3.5 km during August 1998 were observed by lidar over Greece and analyzed [*Formenti et al.*, 2001a, 2002a, 2002b]. *Dulac and Chazette* [2003] present vertical structure observations obtained south of Greece in June 1997 and found several turbid layers at altitudes up to 2 and 4 km; the lowest layer contained pollution aerosols while dust particles were found between about 1.2 to 4 km.

[33] Under such circumstances the continuous and simultaneous observations of aerosol optical properties both in the total atmospheric column and at the surface level can yield valuable information on the aerosol vertical structure in the study region.

4.1.2.1. Aerosol Layer Height

[34] A statistical estimation of the optically active aerosol layer in Northern Greece, at Mount Athos Observatory (MAO), was made by *Formenti et al.* [2001a] and *Gerasopoulos et al.* [2003]. In these studies, the slope H of the regression line ($\tau_{ext} = H \cdot \sigma_{scat} + b$) was derived from the linear relationship between AOT (τ_{ext}) and the surface scattering coefficient (σ_{scat}). This slope provides an estimation of the effective thickness or scale height of the optical active aerosol layer; the variance indicates how well the column extinction is represented by the scattering coefficient measured at surface level.

[35] Assuming that the aerosols in the entire atmospheric column are homogeneously distributed from the surface to an altitude H, then the aerosol concentration does not change with altitude but remains the same as at the surface level. H can be evaluated from the AOT definition as follows:

$$\tau_{ext} = (\sigma_{scat} + \sigma_{abs}) \cdot z, \tag{4}$$

where z is the length of propagation path. Therefore

$$z = \frac{\tau_{ext} \cdot \omega_0}{\sigma_{scat}}. \tag{5}$$

After substitution of σ_{scat} by σ_{scat0}, (σ_{scat0} is the surface scattering coefficient as measured by the nephelometer), we can rewrite equation (5) as

$$H = \frac{\tau_{ext} \cdot \omega_0}{\sigma_{scat0}} \cdot f \cdot g, \tag{6}$$

where τ_{ext} is the aerosol optical thickness of the entire atmospheric column obtained from the AERONET measurements; f is the aerosol drying factor (the aerosol can be dried in the nephelometer due to instrument heating and, as a result, will change scattering properties; $f = 1$ if no drying, otherwise $f < 1$); g is the aerosol measuring efficiency (large particles can be lost during the transport into the nephelometer; $g = 1$ if no losses, otherwise $g < 1$).

[36] Although almucantar retrieved ω_0 values were available from the AERONET database, they were non-
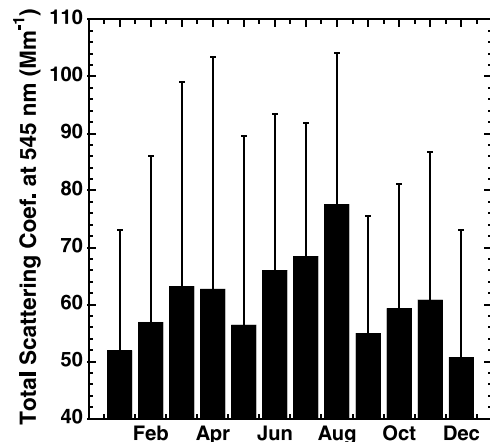

Figure 6. Monthly mean values of total scattering coefficient measured at the surface. Vertical bars indicate standard deviation.

continuous and would limit a time series analysis of H. On the other hand, as was noted in section 4.1.1.3, atmospheric aerosols in the study area are relatively low absorbing and it can be assumed that variation in ω_0 will yield a deviation of H within 10%. The estimation of f and g is more complicated. While the reduction of relative humidity in the Nephelometer can be estimated, the relationship between humidity and scattering properties is very complex, and furthermore there is no information on the vertical humidity profile. The measuring efficiency (g) mainly attributed to loss of coarse dust particles, which may not passing through the intake and resulting underestimate of σ_{scat0} in extremely dust-loaded conditions. However, if we neglect the effects described above, equation (6) can be simplified to

$$H \approx \frac{\tau_{ext}}{\sigma_{scat0}}. \tag{7}$$

This ratio can be used for an estimation of the equivalent aerosol height and reflects the general vertical structure of atmospheric aerosols passing over the site. If the main aerosol concentration is near the surface (aloft), the altitude H will be lowered (extended) and indicate an equivalent aerosol height.

4.1.2.2. Case Study Analysis

[37] During a specific aerosol event the aerosol absorption properties, humidity conditions, and probable loss of particles should be nearly constant and will produce only a bias of H. Thus analysis of specific episodes can provide an example of H behavior as a function of the time.

[38] Two examples have been chosen for detailed analysis. Two days of dust storm (å = −0.003 ± 0.079 (mean ± standard deviation)) on 11−12 May 1996 and two days of anthropogenic pollution haze (å = 1.41 ± 0.04) on 29−30 August 1998. The curves in Figure 7a correspond to the 11−12 May 1996 event, and show the arrival of a high-altitude dust plume during the afternoon of 11 May, with dust settling later, followed by drastic τ_{ext} increases on 12 May. During the morning of 11 May, τ_{ext}^{550} had low values, about 0.2, representing clean sky conditions; H values during this period were about 7 km. From noon, τ_{ext}^{550} increased to about 0.5, causing H to be as high as 19−24 km because of very low surface scattering that remained at about 22 Mm^{-1}. Early morning measurements on 12 May, showed τ_{ext}^{550} about 0.4; however, at the same time H values dropped to 13 km (surface scattering about 30 Mm^{-1}). Afterward, τ_{ext}^{550} sharply increased (1.3−2) during afternoon, and H in that time reaches minimal values of 2−6 km (surface scattering 300−500 Mm^{-1}). The mean values of τ_{ext}^{550}, H, and σ_{scat0} for the entire period analyzed were 0.51 ± 0.49, 7.3 ± 4.2 km, and 125 ± 190 Mm^{-1}, respectively. The air mass backward trajectory ending at 1400 UT (1700 LT) on 11 May (Figure 7c), when H exhibited a peak, suggests a north or northwest Saharan dust origin. Thus the typical arrival of a Saharan dust plume at high altitude and its subsequent settling is shown by the combined H and τ_{ext} time dependence analysis.

[39] For the anthropogenic pollution event during 29−30 August 1998 τ_{ext}^{550} (Figure 7b) was stable and about 0.38 ± 0.03; H indicated a low aerosol layer height and remained at 3.4 ± 1.1 km; the σ_{scat0} for this period was 127 ± 49 Mm^{-1}.

The backward trajectory ending at 1400 UT on 29 August (Figure 7d) shows that the boundary layer air mass originated in Turkey, passed over the Mediterranean Sea and arrived at Sede Boker via central Israel. Therefore, in this case, H indicated an episode of anthropogenic pollution haze, with a monotonous pollution character associated with long-range low-altitude pollution transport.

4.1.2.3. Aerosol Vertical Structure

[40] By using the whole data set of measured τ_{ext} and σ_{scat0} we are able to estimate the general vertical aerosol distribution. Aerosol optical thicknesses for fine (τ_{ext}^{f}) and coarse (τ_{ext}^{c}) fractions characterize an anthropogenic or dust aerosol burden. Thus the relationship between τ_{ext}^{f}, τ_{ext}^{c}, and H will indicate general transport altitudes for anthropogenic aerosols and mineral dust.

[41] The AERONET almucantar retrievals provide values for τ_{ext}^{f} and τ_{ext}^{c}; however, the Sun/sky photometer performs only a few almucantar measurements a day. Moreover, a number of restrictions are applied to the data before the retrieval algorithm is processed. Therefore the final data set for τ_{ext}^{f} and τ_{ext}^{c} is quite limited in comparison with the τ_{ext} retrieved from direct Sun measurements.

[42] In order to extend the data set of τ_{ext}^{f} and τ_{ext}^{c}, the Ångström parameter was used for separating fine and coarse mode components of τ_{ext}. The relationship between the Ångström parameter and the aerosol fine fraction ($\beta = \tau_{ext}^{f}/\tau_{ext}$) were derived on the basis of available almucantar retrievals for the given site. This relationship was then employed for deriving τ_{ext}^{f} and τ_{ext}^{c} from τ_{ext}. The data set obtained was used to adjust the AERONET and nephelometer observations. These data were analyzed for total column τ_{ext}^{f}, τ_{ext}^{c} and the simultaneous variations of the light-scattering coefficient at the surface.

[43] The relationship obtained between the Ångström parameter and aerosol fine fraction (Figure 8), for our site, has the expression of

$$\mathring{a} = 1.49\{\exp(1.0 \cdot \beta) - 1.27\}. \tag{8}$$

The equations for τ_{ext}^{f} and τ_{ext}^{c} can be written as follows:

$$\tau_{ext}^{f} = \beta \cdot \tau_{ext} \tag{9}$$

$$\tau_{ext}^{c} = \tau_{ext} - \tau_{ext}^{f}, \tag{10}$$

where $\beta = \ln(0.67 \cdot \mathring{a} + 1.27)$ and $0 \leq \beta \leq 1$.

[44] Next, the relationship between τ_{ext}^{f}, τ_{ext}^{c} and H was investigated for all simultaneous Sun photometer and nephelometer measurements (Figure 9). This data set shows that H has a low-altitude tendency as τ_{ext}^{f} (pollution) increases and the contribution of τ_{ext}^{c} (dust) decreases, on the other hand, a high-altitude tendency of H attributed to the increase of τ_{ext}^{c} and a decrease in the τ_{ext}^{f} contribution. Figure 9 contains the results of a long series of observations (February 1998 to April 2002) and reflects the general aerosol vertical structure above the Sede Boker site. Because of this site's geographic location, the observations can be considered as representative of the vertical distribution of desert dust plumes and anthropogenic aerosol transport over the Eastern Mediterranean basin.
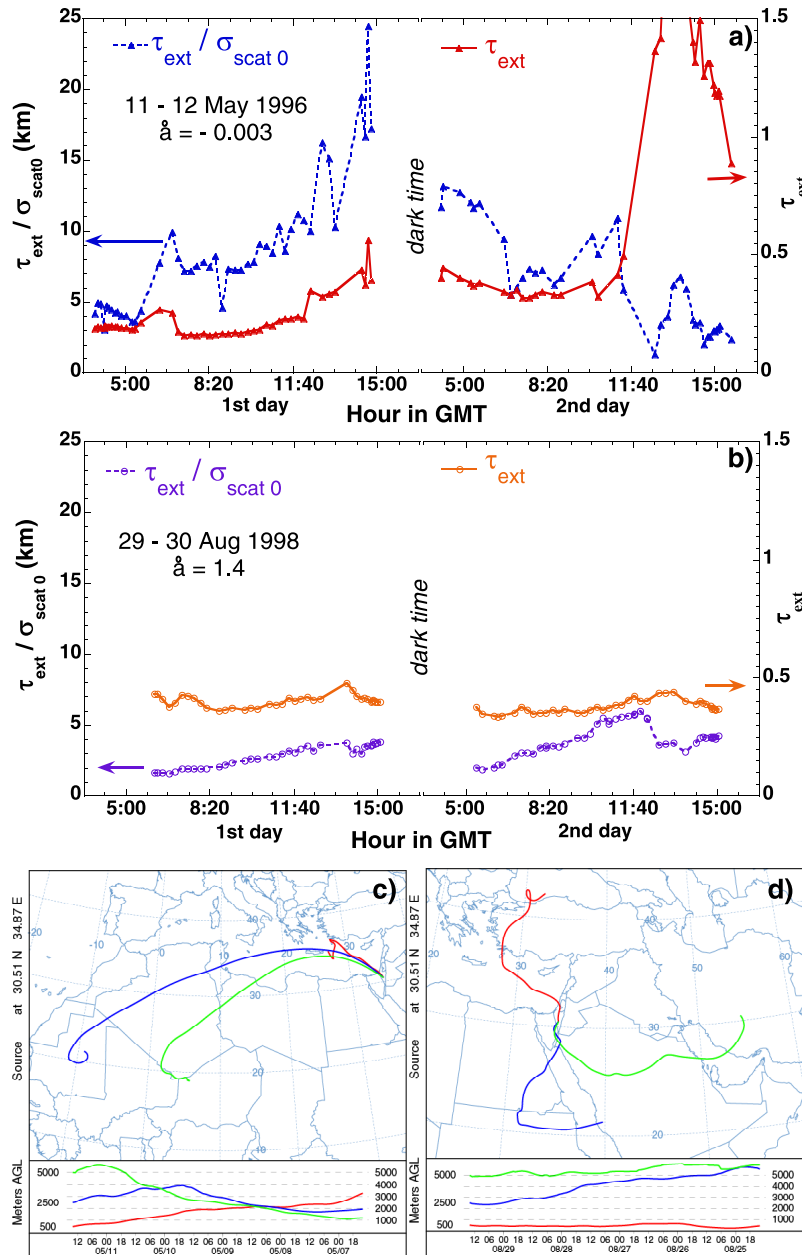
Figure 7. Ratio of $\tau_{ext}/\sigma_{scat0}$ and τ_{ext} time dependence for (a) a dust storm (11–12 May 1996) and (b) anthropogenic pollution haze (29–30 August 1998) and backward trajectory ending at 1400 UT on (c) 11 May 1996 and (d) 29 August 1998.

4.2. Radiative Effect of Dust Versus Pollution

[45] Information about the variability of aerosol optical thickness and the ability to distinguish between dust and anthropogenic pollution aerosols enables attribution of aerosol radiative effect to dust versus anthropogenic aerosol. The direct solar radiative effect of dust and anthropogenic pollution in the spectral range of $0.175–2.270\ \mu$m and under cloud-free conditions (note the mean fractional cloud cover for the study region is 0.29) was assessed by the radiative transfer model CLIRAD-SW [*Chou*, 1992; *Chou and Suarez*, 2002]. The model includes the absorption and scattering due to water vapor, O_3, O_2, CO_2, clouds, and aerosols. The reflection and transmission of a scattering layer are computed using the δ Eddington approximation

and the fluxes are computed using the two-stream adding method. The midlatitude summer atmosphere was chosen as an approximation of temperature, ozone, water vapor profiles, and CO_2 concentration (equal to 350 ppm).

[46] The aerosol radiative effect at the top of the atmosphere (TOA) and at the surface (SFC) was calculated using the definition

$$\Delta F_{TOA} = F_{\uparrow\ TOA}^{clear} - F_{\uparrow\ TOA}^{dust/pollut.}$$

$$\Delta F_{SFC} = F_{\downarrow\ SFC}^{dust/pollut.} - F_{\downarrow\ SFC}^{clear},$$

(11)

where $F_{\uparrow\ TOA}^{clear}$ and $F_{\uparrow\ TOA}^{dust/pollut.}$ are upwelling fluxes at the TOA in no aerosol and aerosol-laden atmospheric condi-
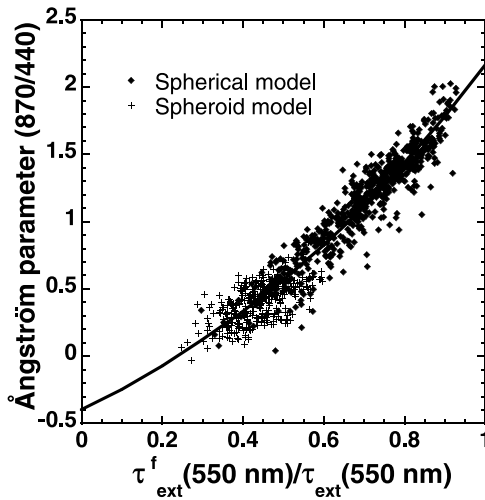
Figure 8. Ångström parameter (870/440) based on spherical model (diamonds) and spheroid model (crosses) almucantar retrievals versus the ratio $\tau_{ext}^{f}/\tau_{ext}$.

tions, respectively; $F_{\downarrow SFC}^{clear}$ and $F_{\downarrow SFC}^{dust/pollut.}$ are downwelling fluxes at the surface level for no aerosol and aerosol-laden conditions, respectively. Thus negative values of ΔF_{TOA} and ΔF_{SFC} correspond to a cooling effect and positive to warming, either at the TOA or at the surface.

[47] The aerosol characteristics (τ_{ext}, ω_0, and asymmetry factor (g)) for different spectral bands of the CLIRAD-SW model (Table 2) were calculated as weighted spectral averages. τ_{ext} was weighted by the spectral solar flux (Φ), ω_0 was weighted by $\tau_{ext} \cdot \Phi$, and g was weighted by $\tau_{ext} \cdot \omega_0 \cdot \Phi$. The spectral dependence of τ_{ext} was obtained from the AERONET data for the analyzed site. The weighted spectral average of τ_{ext} was calculated for three wavelength intervals 0.175 to 0.70 μm, 0.70 to 1.220 μm and 1.220 to 2.270 μm, corresponding to the spectral bands of the CLIRAD-SW model. The weighted spectral averages of ω_0 and g, which have much less influence on radiative effect calculations than spectral τ_{ext}, were subdivided into

only two wavelength intervals, 0.175 to 0.70 μm and 0.70 to 2.270 μm.

[48] Daily averaged aerosol optical thickness caused by dust (τ_{ext}^{dust}) and anthropogenic pollution ($\tau_{ext}^{pollut.}$) was used for radiative effect calculations of the dust and pollution portions. τ_{ext}^{dust} and $\tau_{ext}^{pollut.}$ were obtained from τ_{ext}^{c}, τ_{ext}^{f} (inferred in section 4.1.2.3.) and a ratio between fine and coarse fractions for pure dust episodes $\tau_{ext}^{f\_dust}/\tau_{ext}^{c\_dust}$. Namely,

$$\tau_{ext}^{dust} = \tau_{ext}^{c} \cdot \left(1 + \frac{\tau_{ext}^{f\_dust}}{\tau_{ext}^{c\_dust}}\right) \qquad (12)$$

then

$$\tau_{ext}^{pollut.} = \tau_{ext}^{f} - \tau_{ext}^{c} \cdot \frac{\tau_{ext}^{f\_dust}}{\tau_{ext}^{c\_dust}}. \qquad (13)$$

The value of the ratio $\tau_{ext}^{f\_dust}/\tau_{ext}^{c\_dust}$ was obtained from the series of the mainly pure dust episodes. This series can be seen as a cluster in Figure 9 for which τ_{ext}^{c} is much higher than τ_{ext}^{f} and H indicates middle and high altitudes. The ratio $\tau_{ext}^{f\_dust}/\tau_{ext}^{c\_dust}$ yields value of 0.38 ± 0.03.

[49] The aerosol vertical profiles of anthropogenic pollution and dust also have to be defined for radiative effect calculation. The aerosol profile assumed in the current study is based on previous studies mentioned in section 4.1.2, information about the atmospheric boundary layer that is provided in section 2, and the assumptions that (1) the major concentration of anthropogenic pollution is in the lower troposphere and atmospheric boundary layer, and (2) dust transport is characterized by higher concentrations aloft. The high-altitude dust transport is also confirmed by our analysis of τ_{ext}^{c} and H, by results from the dust prediction system for the study area [*Alpert et al.*, 2002, 2004], and by sporadic lidar observations in the region [*Dulac and Chazette*, 2003]. The total column aerosol optical thickness is assumed to be equally distributed from the surface level up to a height of about 2 km for pollution and 4.5 km for
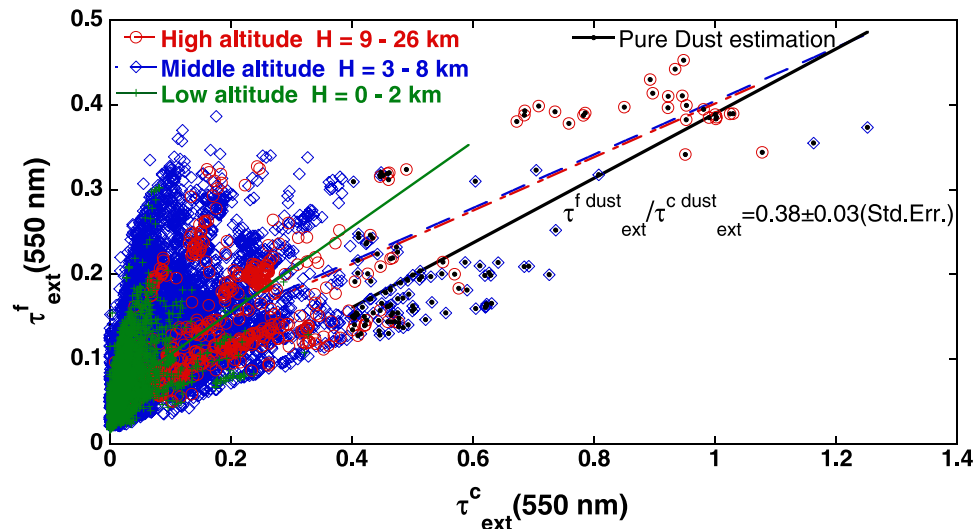

Figure 9. Plot of τ_{ext}^{f} versus τ_{ext}^{c} at 550 nm and relationship with three ranges of aerosol altitudes: low (0−2 km), green crosses; middle (3−8 km), blue diamonds; and high (9−26 km), red circles.

Table 2. Mean ω_0 and g for Dust and Pollution Aerosols for Different Spectral Bands of the CLIRAD-SW Model

Spectral Range, µm	Dust		Pollution	
	$0.175-0.700$	$0.700-2.270$	$0.175-0.700$	$0.700-2.270$
ω_0	0.97	0.98	0.95	0.93
g	0.67	0.66	0.68	0.59

dust. The more detailed profile definition has only a minor influence on the calculations of the aerosol radiative effect.

[50] An average surface reflectance at a wavelength of 0.659 µm for several months was obtained from the Moderate Resolution Imaging Spectroradiometer (MODIS) instrument aboard the Terra satellite. This suggests surface reflectance of about 0.35 for summer, 0.23 for winter and 0.30 for the transition seasons in the Negev desert area.

[51] The lookup tables for the radiative effect of pollution and dust for various surface reflectance and set of solar zenith angles were derived and applied to daily averages of τ_{ext}^{dust} and $\tau_{ext}^{pollut.}$. The aerosol radiative effects for each month were also calculated as an average for the range of appropriate solar zenith angles.

[52] The 24-hour aerosol radiative effect for dust and pollution along with radiative efficiency with respect to optical thickness at 550 nm are presented in Table 3 and Figure 10. Table 3 also shows annual averages for radiative effect and efficiency of observed aerosol for ocean surface reflectance of 0.07. The calculated radiative effect shows negative values during all seasons at the TOA and at the surface, above land and ocean. It also shows a generally dominant role of mineral dust, though the radiative effect of pollution aerosol distinctly exceeds that of mineral dust in August. However, although the $\tau_{ext}^{pollut.}$ is higher during the summer than during the winter, the TOA pollution radiative effect is higher in the winter and between January to March even exceeds the most polluted month, August. The reason for this anomaly is the darker surface reflectance in the winter. This effect can also be strengthened by an increase of aerosol radiative effect for high solar zenith angles.

[53] In a previous study based on measurements at the Sede Boker site, *Andreae et al.* [2002] suggested that pollution aerosols made the largest contribution to radiative effects over the study region. This conclusion coincides with the present analysis only in the case of low dust loading measured through the whole atmospheric column, for example in August. However, for most of the time dust plays a dominant role in the aerosol radiative effects. This difference can be attributed to the fact that these authors had based their analysis on surface data, where pollution loading is most concentrated, while the dust plumes aloft are not adequately sampled at the surface.

[54] Another study of aerosol radiative effect in the Mediterranean region was conducted in the framework of the MINOS experiment [*Markowicz et al.*, 2002]. This study took place along the northeastern shores of Crete (35.34°N, 25.67°E, 265 m above msl), Greece. The radiative effect assessment was based on radiative transfer models and radiation flux measurements; TOA radiative effect was obtained from the CERES instrument. Note that surface effect in the *Markowicz et al.* [2002] study was defined as the effect of aerosol on the net (downwelling minus upwelling) solar flux, which is most relevant for

hydrological cycle studies, while in the current study the surface effect was defined as a difference between downwelling fluxes only. The pollution radiative efficiency at the surface for the MINOS campaign was found to be -85 $Wm^{-2}\tau^{-1}$ and comparable to an -81 $Wm^{-2}\tau^{-1}$ annually averaged radiative efficiency for ocean surface reflectance in the current study. In spite of the small difference in the surface effect between MINOS and Sede Boker data, the TOA effect in Sede Boker (-56 $Wm^{-2}\tau^{-1}$) is larger than in MINOS (-31 $Wm^{-2}\tau^{-1}$). This suggests less absorbing aerosol at Sede Boker. Indeed, the ratio $\Delta F_{SFC}/\Delta F_{TOA}$, which is a measure of aerosol absorbing efficiency, is 2.7 for MINOS and 1.4 for Sede Boker. As noted by *Satheesh and Ramanathan* [2000] and *Markowicz et al.* [2002] a model of sea salt or sulfate aerosol yields a ratio of 1.5. This fact provides support for the dominating radiative role of sulfate aerosols in the eastern Mediterranean region [*Andreae et al.*, 2002; *Haywood and Shine*, 1995].

[55] *Christopher and Zhang* [2002] report instantaneous aerosol radiative effect of -12.6 Wm^{-2} ($\tau_{ext}^{550} = 0.114$) at the TOA derived from MODIS and CERES instruments over the ocean for North African aerosol outflow, most of which is likely to be related to dust. This yields radiative efficiencies of 110 $Wm^{-2}\tau^{-1}$. The corresponding value in this study of instantaneous dust radiative efficiency over the ocean at the TOA is -118 $Wm^{-2}\tau^{-1}$ (not presented in Table 3), and thus comparable to MODIS and CERES observations in the North African outflow. Slightly higher TOA radiative efficiency at Sede Boker can be explained by less absorbing dust [e.g., *Kubilay et al.*, 2003].

5. Conclusions

[56] This paper presents an analysis of the long-term (1995–2003) observations conducted at a crossroads
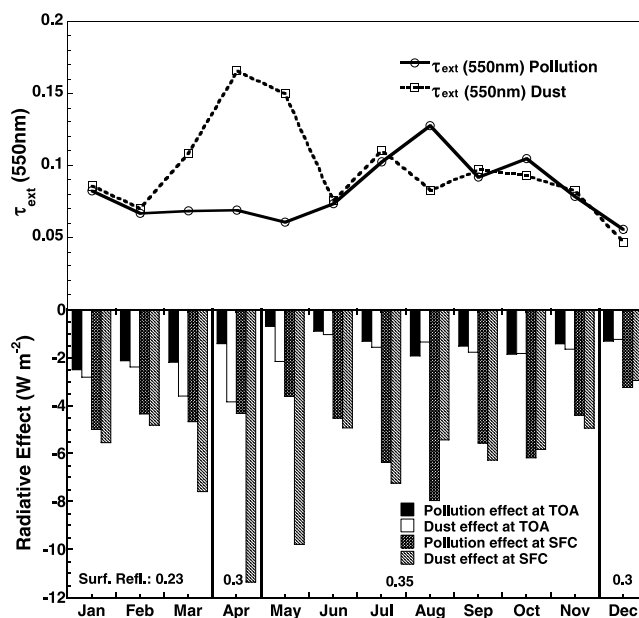

Figure 10. Monthly mean direct aerosol radiative effect of dust and anthropogenic pollution over land, accompanied by means of dust- and pollution-related aerosol optical thickness.

Table 3. Direct 24-Hour Solar Radiative Effect of Dust and Anthropogenic Pollution in the Spectral Range of 0.175–2.270 μm and Cloud-Free Conditions for the Sede Boker Site[a]

Over Land

| | $\tau_{ext}(550)$ | | | TOA | | | | SFC | | | |
	Surface Reflected	Dust	Pollution	Dust DARE, W/m²	Dust RE, W/(m²·AOT)	Pollution DARE, W/m²	Pollution RE, W/(m²·AOT)	Dust DARE, W/m²	Dust RE, W/(m²·AOT)	Pollution DARE, W/m²	Pollution RE, W/(m²·AOT)
Jan.	0.23	0.086	0.082	-2.8	-33	-2.5	-31	-5.5	-65	-5.0	-61
Feb.	0.23	0.070	0.067	-2.4	-34	-2.1	-32	-4.8	-69	-4.3	-65
March	0.23	0.108	0.068	-3.6	-33	-2.2	-32	-7.6	-70	-4.7	-68
April	0.30	0.165	0.069	-3.8	-23	-1.4	-21	-11.4	-69	-4.3	-63
May	0.35	0.150	0.061	-2.2	-14	-0.7	-12	-9.8	-65	-3.6	-60
June	0.35	0.075	0.073	-1.0	-14	-0.9	-12	-4.9	-65	-4.5	-62
July	0.35	0.110	0.102	-1.6	-14	-1.3	-13	-7.2	-66	-6.4	-62
Aug.	0.35	0.083	0.127	-1.4	-16	-1.9	-15	-5.4	-65	-8.0	-62
Sept.	0.35	0.097	0.092	-1.8	-18	-1.5	-17	-6.3	-65	-5.6	-61
Oct.	0.35	0.093	0.105	-1.8	-20	-1.9	-18	-5.8	-63	-6.2	-59
Nov.	0.35	0.082	0.078	-1.7	-20	-1.4	-18	-4.9	-60	-4.4	-56
Dec.	0.30	0.046	0.055	-1.2	-27	-1.3	-24	-3.0	-64	-3.2	-59
Average		0.097	0.082	-2.1	-22	-1.6	-20	-6.4	-65	-5.0	-62

Over Ocean

| | $\tau_{ext}(550)$ | | | TOA | | | | SFC | | | |
	Surface Reflected	Dust	Pollution	Dust DARE, W/m²	Dust RE, W/(m²*AOT)	Pollution DARE, W/m²	Pollution RE, W/(m²*AOT)	Dust DARE, W/m²	Dust RE, W/(m²*AOT)	Pollution DARE, W/m²	Pollution RE, W/(m²*AOT)
Annual Average	0.07	0.097	0.082	-5.9	-60	-4.6	-56	-8.4	-86	-6.6	-81

[a]DARE is Direct Aerosol Radiative Effect; RE is radiative efficiency (RE = DARE/τ_{ext}(550)).

between dust and pollution aerosol sources in Israel's Negev desert. Seasonal variability of aerosol optical properties, mass concentrations, vertical profile structure, and dust versus pollution radiative effect have been studied and quantified. Results may contribute to the long-term tracking of environmental change, the understanding of global climate change, and prediction modeling. Below is a summary of our main results and conclusions.

[57] 1. Variability of aerosol optical thickness, total scattering coefficient, size parameters, and mass concentrations were found to be related to the synoptic seasons. The seasonal aerosol optical properties show a quite consistent periodic variability throughout the seven years of data analyzed.

[58] 2. The monthly mean τ_{ext}^{500} ranged from a minimum value of 0.11 ± 0.06 during December to a maximum of 0.25 ± 0.15 during April. The frequency of occurrence histogram of daily mean τ_{ext}^{500} reached a maximum of 0.15 to 0.20.

[59] 3. The total scattering coefficient, σ_{scat0}, during August showed a maximum monthly mean value of 78 ± 53 Mm^{-1} (at 545 nm) and was similar to that of moderately polluted continental air masses [Andreae et al., 2002]. The overall mean value was 60 ± 56 Mm^{-1}.

[60] 4. A ratio of the entire atmospheric column aerosol optical thickness to the total scattering coefficient at surface level could be used to estimate the aerosol vertical structure. This demonstrated that long-range dust transport occurred at high altitudes while anthropogenic pollution is transported at lower altitudes.

[61] 5. Negative radiative effect by dust and anthropogenic aerosol at the TOA and at the surface took place during the whole year. Results show that in most of the cases the dominating component that affects the radiative regime in the study area is mineral dust; however, the anthropogenic component is also pronounced.

References

Alpert, P., S. O. Krichak, M. Tsidulko, H. Shafir, and J. H. Joseph (2002), A dust prediction system with TOMS initialization, *Mon. Weather Rev.*, 130(9), 2335–2345.

Alpert, P., P. Kishcha, A. Shtivelman, S. O. Krichak, and J. H. Joseph (2004), Vertical distribution of Saharan dust based on 2.5-year model predictions, *Atmos. Res.*, 70(2), 109–130.

Anderson, T. L., and J. A. Ogren (1998), Determining aerosol radiative properties using the TSI 3563 integrating nephelometer, *Aerosol Sci. Technol.*, 29(1), 57–69.

Anderson, T. L., et al. (1996), Performance characteristics of a high-sensitivity, three-wavelength, total scatter/backscatter nephelometer, *J. Atmos. Oceanic Technol.*, 13(5), 967–986.

Andreae, T. W., M. O. Andreae, C. Ichoku, W. Maenhaut, J. Cafmeyer, A. Karnieli, and L. Orlovsky (2002), Light scattering by dust and anthropogenic aerosol at a remote site in the Negev desert, Israel, *J. Geophys. Res.*, 107(D2), 4008, doi:10.1029/2001JD900252.

Charlson, R. J., S. E. Schwartz, J. M. Hales, R. D. Cess, J. A. Coakley, J. E. Hansen, and D. J. Hofmann (1992), Climate forcing by anthropogenic aerosols, *Science*, 255(5043), 423–430.

Chou, M. D. (1992), A solar-radiation model for use in climate studies, *J. Atmos. Sci.*, 49(9), 762–772.

Chou, M. D., and M. J. Suarez (2002), A solar radiation parameterization for atmospheric studies, Lab. for Atmos., NASA Goddard Space Flight Cent., Greenbelt, Md.

Christopher, S. A., and J. L. Zhang (2002), Shortwave aerosol radiative forcing from MODIS and CERES observations over the oceans, *Geophys. Res. Lett.*, 29(18), 1859, doi:10.1029/2002GL014803.

Chu, D. A., Y. J. Kaufman, G. Zibordi, J. D. Chern, J. Mao, C. Li, and B. N. Holben (2003), Global monitoring of air pollution over land from the Earth Observing System-Terra Moderate Resolution Imaging Spectroradiometer (MODIS), *J. Geophys. Res.*, 108(D21), 4661, doi:10.1029/2002JD003179.

Dayan, U., and J. Rodnizki (1999), The temporal behavior of the atmospheric boundary layer in Israel, *J. Appl. Meteorol.*, 38(6), 830–836.

di Sarra, A., T. Di Iorio, M. Cacciani, G. Fiocco, and D. Fua (2001), Saharan dust profiles measured by lidar at Lampedusa, *J. Geophys. Res.*, 106(D10), 10,335–10,347.

Draxler, R. R., and G. D. Hess (1998), An overview of the Hysplit_4 modeling system for trajectories, *Aust. Meteorol. Mag.*, 47, 295–308.

Dubovik, O., and M. D. King (2000), A flexible inversion algorithm for retrieval of aerosol optical properties from Sun and sky radiance measurements, *J. Geophys. Res.*, 105(D16), 20,673–20,696.

Dubovik, O., A. Smirnov, B. N. Holben, M. D. King, Y. J. Kaufman, T. F. Eck, and I. Slutsker (2000), Accuracy assessments of aerosol optical properties retrieved from Aerosol Robotic Network (AERONET) Sun and sky radiance measurements, *J. Geophys. Res.*, 105(D8), 9791–9806.

Dubovik, O., B. Holben, T. F. Eck, A. Smirnov, Y. J. Kaufman, M. D. King, D. Tanre, and I. Slutsker (2002a), Variability of absorption and optical properties of key aerosol types observed in worldwide locations, *J. Atmos. Sci.*, 59(3), 590–608.

Dubovik, O., B. N. Holben, T. Lapyonok, A. Sinyuk, M. I. Mishchenko, P. Yang, and I. Slutsker (2002b), Non-spherical aerosol retrieval method employing light scattering by spheroids, *Geophys. Res. Lett.*, 29(10), 1415, doi:10.1029/2001GL014506.

Dulac, F., and P. Chazette (2003), Airborne study of a multi-layer aerosol structure in the eastern Mediterranean observed with the airborne polarized lidar ALEX during a STAAARTE campaign (7 June 1997), *Atmos. Chem. Phys.*, 3, 1817–1831.

Formenti, P., et al. (2001a), Aerosol optical properties and large-scale transport of air masses: Observations at a coastal and a semiarid site in the eastern Mediterranean during summer 1998, *J. Geophys. Res.*, 106(D9), 9807–9826.

Formenti, P., et al. (2001b), Physical and chemical characteristics of aerosols over the Negev desert (Israel) during summer 1996, *J. Geophys. Res.*, 106(D5), 4871–4890.

Formenti, P., et al. (2002a), STAAARTE-MED 1998 summer airborne measurements over the Aegean Sea: 2. Aerosol scattering and absorption, and radiative calculations, *J. Geophys. Res.*, 107(D21), 4551, doi:10.1029/2001JD001536.

Formenti, P., et al. (2002b), STAAARTE-MED 1998 summer airborne measurements over the Aegean Sea: 1. Aerosol particles and trace gases, *J. Geophys. Res.*, 107(D21), 4550, doi:10.1029/2001JD001337.

Ganor, E. (1994), The frequency of Saharan dust episodes over Tel-Aviv, Israel, *Atmos. Environ.*, 28(17), 2867–2871.

Ganor, E., and H. A. Foner (2001), Mineral dust concentrations, deposition fluxes and deposition velocities in dust episodes over Israel, *J. Geophys. Res.*, 106(D16), 18,431–18,437.

Gerasopoulos, E., M. O. Andreae, C. S. Zerefos, T. W. Andreae, D. Balis, P. Formenti, P. Merlet, V. Amiridis, and C. Papastefanou (2003), Climatological aspects of aerosol optical properties in northern Greece, *Atmos. Chem. Phys.*, 3, 2025–2041.

Hamonou, E., P. Chazette, D. Balis, F. Dulac, X. Schneider, E. Galani, G. Ancellet, and A. Papayannis (1999), Characterization of the vertical structure of Saharan dust export to the Mediterranean basin, *J. Geophys. Res.*, 104(D18), 22,257–22,270.

Hansen, J., M. Sato, and R. Ruedy (1997), Radiative forcing and climate response, *J. Geophys. Res.*, 102(D6), 6831–6864.

Haywood, J. M., and K. P. Shine (1995), The effect of anthropogenic sulfate and soot aerosol on the clear-sky planetary radiation budget, *Geophys. Res. Lett.*, 22(5), 603–606.

Holben, B. N., T. F. Eck, I. Slutsker, D. Tanre, J. P. Buis, A. Setzer, E. Vermote, J. A. Reagan, Y. J. Kaufman, and T. Nakajima (1998), AERONET—A federated instrument network and data archive for aerosol characterization, *Remote Sens. Environ.*, 66(1), 1–16.

Ichoku, C., et al. (1999), Interrelationships between aerosol characteristics and light scattering during late winter in an eastern Mediterranean arid environment, *J. Geophys. Res.*, 104(D20), 24,371–24,393.

Israelevich, P. L., E. Ganor, Z. Levin, and J. H. Joseph (2003), Annual variations of physical properties of desert dust over Israel, *J. Geophys. Res.*, 108(D13), 4381, doi:10.1029/2002JD003163.

Kaufman, Y. J., and R. S. Fraser (1997), The effect of smoke particles on clouds and climate forcing, *Science*, *277*(5332), 1636–1639.

Kaufman, Y. J., A. Gitelson, A. Karnieli, E. Ganor, R. S. Fraser, T. Nakajima, S. Mattoo, and B. N. Holben (1994), Size distribution and scattering phase function of aerosol particles retrieved from sky brightness measurements, *J. Geophys. Res.*, *99*(D5), 10,341–10,356.

Kaufman, Y. J., D. Tanre, and O. Boucher (2002), A satellite view of aerosols in the climate system, *Nature*, *419*(6903), 215–223.

Kubilay, N., T. Cokacar, and T. Oguz (2003), Optical properties of mineral dust outbreaks over the northeastern Mediterranean, *J. Geophys. Res.*, *108*(D21), 4666, doi:10.1029/2003JD003798.

Lelieveld, J., et al. (2002), Global air pollution crossroads over the Mediterranean, *Science*, *298*(5594), 794–799.

Levin, Z., E. Ganor, and V. Gladstein (1996), The effects of desert particles coated with sulfate on rain formation in the eastern Mediterranean, *J. Appl. Meteorol.*, *35*(9), 1511–1523.

Maenhaut, W., I. Salma, J. Cafmeyer, H. J. Annegarn, and M. O. Andreae (1996a), Regional atmospheric aerosol composition and sources in the eastern Transvaal, South Africa, and impact of biomass burning, *J. Geophys. Res.*, *101*(D19), 23,631–23,650.

Maenhaut, W., R. Salomonovic, J. Cafmeyer, C. Ichoku, A. Karnieli, and M. O. Andreae (1996b), Anthropogenic and natural radiatively active aerosol types at Sede Boker, Israel, *J. Aerosol Sci.*, *27*, suppl. 1, S47–S48.

Maenhaut, W., J. Cafmeyer, J. Ptasinski, M. O. Andreae, T. W. Andreae, W. Elbert, F. X. Meixner, A. Karnieli, and C. Ichoku (1997), Chemical composition and light scattering of the atmospheric aerosol at a remote site in the Negev desert, Israel, *J. Aerosol Sci.*, *28*, suppl. 1, S73–S74.

Markowicz, K. M., P. J. Flatau, M. V. Ramana, P. J. Crutzen, and V. Ramanathan (2002), Absorbing Mediterranean aerosols lead to a large reduction in the solar radiation at the surface, *Geophys. Res. Lett.*, *29*(20), 1968, doi:10.1029/2002GL015767.

Menon, S., J. Hansen, L. Nazarenko, and Y. F. Luo (2002), Climate effects of black carbon aerosols in China and India, *Science*, *297*(5590), 2250–2253.

Reid, J. S., et al. (2003), Comparison of size and morphological measurements of coarse mode dust particles from Africa, *J. Geophys. Res.*, *108*(D19), 8593, doi:10.1029/2002JD002485.

Rosenfeld, D., Y. Rudich, and R. Lahav (2001), Desert dust suppressing precipitation: A possible desertification feedback loop, *Proc. Natl. Acad. Sci. U. S. A.*, *98*(11), 5975–5980.

Satheesh, S. K., and V. Ramanathan (2000), Large differences in tropical aerosol forcing at the top of the atmosphere and Earth's surface, *Nature*, *405*(6782), 60–63.

Smirnov, A., B. N. Holben, T. F. Eck, O. Dubovik, and I. Slutsker (2000), Cloud-screening and quality control algorithms for the AERONET database, *Remote Sens. Environ.*, *73*(3), 337–349.

Sobanska, S., C. Coeur, W. Maenhaut, and F. Adams (2003), SEM-EDX characterisation of tropospheric aerosols in the Negev desert (Israel), *J. Atmos. Chem.*, *44*(3), 299–322.

Stern, E., Y. Gradus, A. Meir, S. Krakover, and H. Tsoar (1986), *Atlas of the Negev*, Keterpress Enterprises, Jerusalem.

Tsidulko, M., S. O. Krichak, P. Alpert, O. Kakaliagou, G. Kallos, and A. Papadopoulos (2002), Numerical study of a very intensive eastern Mediterranean dust storm, 13–16 March 1998, *J. Geophys. Res.*, *107*(D21), 4581, doi:10.1029/2001JD001168.

Wang, J., and S. A. Christopher (2003), Intercomparison between satellite-derived aerosol optical thickness and $PM_{2.5}$ mass: Implications for air quality studies, *Geophys. Res. Lett.*, *30*(21), 2095, doi:10.1029/2003GL018174.

————————

M. O. Andreae and T. W. Andreae, Biogeochemistry Department, Max Planck Institute for Chemistry, P.O. Box 3060, D-55020 Mainz, Germany.

Y. Derimian and A. Karnieli, Remote Sensing Laboratory, Jacob Blaustein Institute for Desert Research, Ben-Gurion University of the Negev, Sede Boker Campus 84990, Israel. (derimian@bgu.ac.il)

O. Dubovik, B. N. Holben, and Y. J. Kaufman, NASA Goddard Space Flight Center, Greenbelt, MD 20771, USA.

I. Koren, Department of Environmental Sciences, Weizmann Institute, Rehovot 76100, Israel.

W. Maenhaut, Department of Analytical Chemistry, Institute for Nuclear Sciences, Ghent University, Proeftuinstraat 86, B-9000 Ghent, Belgium.